

OPEN ACCESS**Repository of the Max Delbrück Center for Molecular Medicine (MDC)
in the Helmholtz Association**

<http://edoc.mdc-berlin.de/15313>

Magnetic resonance thermometry: methodology, pitfalls and practical solutions

Winter, L. and Oberacker, E. and Paul, K. and Ji, Y. and Oezerdem, C. and Ghadjar, P. and Thieme, A. and Budach, V. and Wust, P. and Niendorf, T.

This is an Accepted Manuscript of an article published by Taylor & Francis in *International Journal of Hyperthermia* on February 2016, available online:

<http://www.tandfonline.com/doi/full/10.3109/02656736.2015.1108462>

The original article has been published in final edited form in:

International Journal of Hyperthermia
2016 FEB; 32(1): 63-75
2015 DEC 27 (first published online)
doi: [10.3109/02656736.2015.1108462](https://doi.org/10.3109/02656736.2015.1108462)

Publisher: [Taylor & Francis](#)

Copyright © 2016 Taylor & Francis

Magnetic Resonance Thermometry: Methodology, Pitfalls and Practical Solutions

Lukas Winter¹, Eva Oberacker¹, Katharina Paul¹, Yiyi Ji¹, Celal Oezerdem¹, Pirus Ghadjar², Alexander Thieme², Volker Budach², Peter Wust² and Thoralf Niendorf^{1,3,4}

¹ Berlin Ultrahigh Field Facility (B.U.F.F.), Max-Delbrück Center for Molecular Medicine, Berlin, Germany

² Department of Radiation Oncology, Charité Universitätsmedizin, Berlin, Germany

³ Experimental and Clinical Research Center (ECRC), a joint cooperation between the Charité Medical Faculty and the Max-Delbrueck Center for Molecular Medicine, Berlin, Germany

⁴ MRI.TOOLS GmbH, Berlin, Germany

Corresponding Author:

Dr. Lukas Winter,
Berlin Ultrahigh Field Facility (B.U.F.F.)
Max-Delbrück Center for Molecular Medicine
Robert-Roessle-Strasse 10
13125 Berlin
Germany
Tel.: +4930 9406 4546
Fax.: +4930 9406 4517;
E-mail: Lukas.Winter@mdc-berlin.de

Word count: 5531

Running Title: Magnetic Resonance Thermometry

Abstract

Clinically established thermal therapies like thermo ablative approaches or adjuvant hyperthermia treatment rely on accurate thermal dose information for the evaluation and adaptation of the thermal therapy. Intratumoral temperature measurements have been correlated successfully with clinical endpoints. Magnetic resonance imaging is the most suitable technique for non-invasive thermometry avoiding complications related to invasive temperature measurements. Since the advent of MR thermometry two decades ago, numerous MR thermometry techniques have been developed continuously increasing accuracy and robustness for *in vivo* applications. While this progress was primarily focused on relative temperature mapping, current and future efforts will likely close the gap towards quantitative temperature readings. These efforts are essential to benchmark thermal therapy efficiency, understand temperature related biophysical and physiological processes and to use these insights to set new landmarks for diagnostic and therapeutic applications. With that in mind, this review summarizes and discusses advances in MR thermometry providing practical considerations, pitfalls and technical obstacles constraining temperature measurement accuracy, spatial and temporal resolution *in vivo*. Established approaches and current trends in thermal therapy hardware are surveyed with respect to potential benefits for MR thermometry.

Background

Thermal therapies can be classified into two groups: (i) thermo ablative approaches with tissue temperatures above 50°C and hyperthermia covering tissue temperatures of 40-45°C. Invasive methods for thermal ablation include laser induced thermal therapy (LITT), radio frequency (RF) ablation or cryoablation (1, 2). Non-invasive thermo-ablative approaches involve high-intensity focused ultrasound (HIFU). Magnetic resonance (MR) guided focused ultrasound (MRgFUS) can be attributed to either group depending on the clinical indication. Clinical treatment of MRgFUS include breast, bone, liver, prostate and brain tumors, uterine fibroids, neuropathic pain as well as movement disorders like essential tremor and Parkinson tremor (3-6). Regional hyperthermia (RHT) is a well-established non-ablative approach which is of clinical value as an adjunct to radio- and/or chemotherapy (7). RHT has been demonstrated to improve local control in various locally advanced tumors in a number of phase II- and phase III-trials (1). Intratumoral temperature measurements of the applied thermal dose have been correlated successfully with clinical endpoints (8-11).

While accurate thermometry is crucial for hyperthermia treatment, invasive thermometry was put into question at an early stage of the development process (12, 13). Potential complications such as hemorrhage, infections or neurological complaints, and other discomfort were observed along with a low acceptance in patients and physicians (12). Driven by this shortcoming, investigators explored surrogates of invasive thermometry. Two principle strategies were suggested including minimal-invasive thermometry utilizing specified anatomic reference points or tracks in hollow organs such as the rectum, vagina, bladder or urethra. Minimal invasive thermometry has demonstrated to be competitive with invasive measurements in pelvic tumors (14-16). Alternatively, the traits of magnetic resonance imaging (MRI) were put to good use for non-invasive thermography. Because of its spatial resolution and anatomic coverage per unit time MRI appears most suitable for non-invasive thermometry versus other physical approaches including impedance tomography, microwave imaging, computed tomography or ultrasound (16). Since the advent of MR thermometry (17, 18), the first decade of development culminated in techniques allowing for qualitative temperature assessment in thermal therapies (19-21). The second decade of

development advanced the capabilities of MR thermometry towards more robust and reliable *in vivo* applications (22-25). The future target of MR thermometry developments is clearly formed around novel methodology and hardware that supports accurate absolute temperature readings *in vivo* with the current developments already pushing into this direction (26-31). These efforts are essential to benchmark thermal therapy efficiency, understand temperature related biophysical and physiological processes and to use these insights for defining and setting new landmarks for diagnostic and therapeutic capabilities.

Recognizing the technical advances and clinical opportunities of MR thermometry this review is an attempt to make the (bio)medical and diagnostic imaging communities aware of these developments, so as to engage the interest of potential clinical adopters, to inspire collaborations across disciplinary boundaries and to attract basic scientists, engineers, hardware professionals, translational researchers, applied scientists and new entrants into the field. In the sections that follow, examples of enabling MR thermometry technology and their applications are provided. Advances in temperature mapping methodology are discussed together with practical considerations and potential pitfalls. Technical obstacles constraining temperature measurement accuracy, spatial and temporal resolution of thermal ablation and hyperthermia treatments are considered. Established approaches and current trends in thermal MR hardware are surveyed together with their practical implications for accurate MR thermometry. A concluding section ventures a glance beyond the horizon and explores future directions. Of course, MR thermometry is an area of vigorous ongoing research, and many potentially valuable developments will receive only brief mention here.

Overview of PRF Thermometry

Numerous MR parameters are sensitive to temperature changes. This includes but is not limited to proton density (32), T_1 relaxation (33, 34), T_2 relaxation (35, 36), apparent water diffusion (37, 38) and magnetization transfer (39). The merits and limitations of MR thermometry based upon these MR parameters are surveyed in an excellent review (40).

Proton resonance frequency (PRF) is another viable temperature dependent MR parameter, which is commonly applied for *in vivo* MR thermometry mapping (20, 41, 42). The resonance frequency of hydrogen nuclei is proportional to the magnetic field $\vec{B}_{loc}(\vec{r})$ at location \vec{r} . The relationship of the applied static magnetic field \vec{B}_0 of an MR scanner to the macroscopic magnetic field \vec{B}_{mac} inside weakly magnetic materials ($|\chi| < 1$) like human tissue to the final local magnetic field \vec{B}_{loc} , is governed by the Maxwell equations (42). Assuming a sphere with a volume magnetic susceptibility χ for macroscopic screening (molecules at a large distance of the proton of interest) and a sphere with the screening constant σ for microscopic screening (hydrogen bound molecule itself and its near neighbors), the relationship between \vec{B}_{loc} , \vec{B}_{mac} and $\vec{B}_0 = B_0 \vec{e}_z$ can be written as (42):

$$\vec{B}_{loc} \cong \vec{B}_{mac} - \left(\frac{2\chi}{3} + \sigma \right) \vec{B}_0 \quad (1)$$

The electron screening of water σ_{water} increases linearly in the temperature range of thermal ablations and hyperthermia with $d\sigma_{water}/dT = 0.01 \text{ ppm}/^\circ\text{C}$, which decreases the chemical shift $\delta[\text{ppm}] = (\sigma_{ref} - \sigma) \cdot 10^6$ (41). It can be used to calculate relative temperature changes ΔT via phase difference $\Delta\varphi$ measurements to a reference phase φ_{ref} at temperature T_{ref} (43):

$$\Delta\varphi = \varphi - \varphi_{ref} = -\gamma TE (B_{loc}(T) - B_{loc}(T_{ref})) = -\gamma TE (\Delta B_{mac} - \left(\frac{2}{3} \Delta\chi + \Delta\sigma \right) B_0) \quad (2)$$

With the gyromagnetic ratio γ , echo time TE , $\Delta B_{mac} = B_{mac}(T) - B_{mac}(T_{ref})$ and temperature induced changes in proton electron screening $\Delta\sigma$ and magnetic volume susceptibility $\Delta\chi$. Neglecting the influence of magnetic volume susceptibilities, the temperature can be derived from:

$$\Delta T = \frac{\Delta \varphi}{\alpha \cdot \gamma \cdot TE \cdot B_0} \quad (3)$$

with the proportionality constant $\alpha = d\sigma/dT$. Apart from adipose tissue, α is relatively independent of tissue type and found in the range of 0.009-0.01ppm/°C (44, 45). With the characteristics of excellent linearity and sensitivity of the proton electron screening in the investigated temperature range and the advantages of phase over magnitude measurements with a) robustness towards B_1 inhomogeneity and b) the ability to use fast imaging techniques like gradient echoes, the PRF method is the most suitable and widely used technique for non-invasive MR thermometry *in vivo* (40).

Pitfalls and Practical Solutions

Notwithstanding the ubiquity and success of PRF thermometry, multiple technical, physical and biophysical challenges remain, which need to be addressed. The technical challenges include magnetic field drift of the MR magnet over time and spatio-temporal resolution constraints. Physical challenges are temperature dependent changes in relative permittivity, electric conductivity and magnetic susceptibility as well as field strength dependent implications on the imaging techniques used. Biophysical challenges include tissue dependent chemical shift, tissue perfusion and diffusion changes. Respiratory motion and cardiac activity constitute physiological constraints that govern the accuracy of PRF MR thermometry but also dictate the viable window of data acquisition. An overview of some relevant parameters influencing the temperature error is outlined in Table I. Equipped with the basic methodology of PRF based MR thermometry the sections that follow discuss these pitfalls and provide practical solutions for *in vivo* applications.

Static magnetic field B_0

The static magnetic field may vary over the time course of a thermal therapy. This is in particular relevant for the PRF method which is very sensitive to magnetic field changes ($\sim 0.01 \text{ ppm}/^\circ\text{C}$ in aqueous tissue) and relies on a phase difference calculation to a reference map. Assuming a constant temperature and a magnetic field drift of 0.02 ppm/h would generate an error of $\pm 2^\circ\text{C}$ over one hour. Corrections of the field drift can be performed by using external reference probes with a known temperature like the water bolus typically surrounding the patient in RF hyperthermia treatment (46). Alternatively, lipids are commonly employed as a reference since their chemical shift is largely immune to temperature changes (19, 21, 47). Internal references like unheated tissue regions (48) or fatty tissue (49) can also be used for drift correction. An example of an *in vivo* PRF map using fatty tissue for correction is illustrated in Figure 1a. After suitable regions of adipose tissue have been labeled, phase correction is performed fitting linear or higher order functions to the phase information in the selected fat regions (49).

Chemical Shift

The temperature dependent chemical shift has a small tissue dependence in the range of published values $-(0.009-0.01)\text{ppm}/^{\circ}\text{C}$ (except adipose tissue) (44, 45) (Table I), which leads to a reasonably small temperature error. In phantom heating experiments, which are performed for RF safety testing or evaluation of MR thermometry methods, high temperature reading accuracies are desirable. Depending on the phantom the proportionality constant α can exhibit higher deviations from pure water literature values leading to inaccuracies in temperature readings. A calibration procedure with accurate fiber tracking and monitoring of the temperature evolution at different locations can reduce the maximum temperature error significantly, e.g. from $\sim 2.2^{\circ}\text{C}$ to $\sim 0.2^{\circ}\text{C}$ (50).

In contrast, the lipid resonance frequency exhibits only a minor temperature dependent chemical shift of $-0.00018\text{ ppm}/^{\circ}\text{C}$ ((51), Table I) making it elusive of using the PRF method for accurate temperature mapping in fat. For voxels containing both water and fat, where the phase is a sum of both signals, temperature errors increase. Solutions are provided with water and fat separated thermal (WAFI) MRI using Dixon chemical shift based fat-water separation to correct for some of the temperature errors while using the fat signal as an internal reference (52). This approach reaches a temperature accuracy as good as $-0.09\pm 0.34^{\circ}\text{C}$ in homogeneous phantoms (53). Fat suppression techniques can be employed using spectral selective RF pulses or inversion recovery techniques with the evolution time being adjusted based upon the T_1 relaxation time of fat (54). These techniques are sensitive to inhomogeneities in the transmission field which is pronounced at higher magnetic field strengths (55). Water selective excitation using spatial-spectral (SPSP) RF pulses is another option to suppress lipid signal contributions and to reduce sensitivity to B_1 inhomogeneities (56-59).

In general lipid suppression is promising at higher magnetic fields B_0 due to a higher chemical shift between water and fat ($\sim 1000\text{Hz}$ at $B_0=7.0\text{T}$). An intriguing approach exploiting this characteristic has been demonstrated at 7.0 T using a frequency selective asymmetric spin-echo based echo planar imaging (EPI) technique (28). This approach employed a slice

selection gradient reversal methodology for fat suppression. The gradient reversal using gradients of differing polarity for excitation and refocusing together with bandwidth-time product changes of the radiofrequency pulses allowed imaging of on-resonant species and suppression of off-resonant species (28). This approach yielded an *in vivo* temperature stability in the human brain of $-0.1 \pm 0.3^\circ\text{C}$ (28).

Electromagnetic tissue properties

Temperature dependent changes in the electromagnetic properties of tissue might have various implications. An increasing temperature decreases the relative permittivity ($\sim 0.5\%/^\circ\text{C}$ for water (60)) and increases the electric conductivity ($\sim 1.7\%/^\circ\text{C}$ for dog muscle (61)) of tissue, which both have implications on phase velocity v_p in a lossy medium or tissue:

$$v_p = \sqrt{\frac{2}{\mu\epsilon}} \left[\sqrt{1 + \left(\frac{\sigma_{el}}{\omega\epsilon}\right)^2} + 1 \right]^{-1/2} \quad (4)$$

With the absolute permittivity ϵ , the permeability μ , the angular frequency ω and the electrical conductivity σ_{el} . This leads to changes in transmit (B_1^+) and receive (B_1^-) phase due to alterations in phase propagation speed (Equation 4) (60). While this effect is mostly significant in larger heating volumes like in deep regional RF hyperthermia, it can be corrected easily utilizing a double echo-method correcting the generated echo time dependent temperature coefficient (60). The extension of Equation 3 allows for a simple correction of this effect:

$$\Delta T_{corr} = \frac{(\Delta\varphi_{sample}(TE_2) - \Delta\varphi_{sample}(TE_1)) - (\Delta\varphi_{ref}(TE_2) - \Delta\varphi_{ref}(TE_1))}{\gamma\alpha B_0(TE_2 - TE_1)} \quad (5)$$

with φ_{ref} being a reference unaffected by temperature change (water bolus) or resonance frequency shift (fat) in order to compensate for the B_0 field drift over time. The temperature error due to phase retardation is relatively constant for low and high field MR applications (60).

In addition to the aforementioned changes in phase velocity, relative permittivity and electric conductivity changes might further influence B_1^+ and B_1^- . This effect is a consequence of direct power losses due to increased electrical conductivity (*power loss density* $\propto \sigma_{el}$) (60) as well as changes in tissue impedance, which determines RF coil loading. Depending on the RF coil type and its sensitivity to these changes and the heated volume, this might influence the scattering parameters increasing total reflected power and/or coupling in multi-channel arrays modifying B_1 amplitude and phase distribution.

The permeability μ or magnetic susceptibility χ of tissue with the relation $\mu = \mu_0 \mu_r = \mu_0 (\chi + 1)$ is also temperature dependent and influences phase velocity (Equation 4). However the temperature increase of the permeability is rather low ($3 \times 10^{-7} \%/^{\circ}\text{C}$ for pure water) as compared to temperature induced changes in permittivity and conductivity and hence can be neglected (60).

Magnetic susceptibility

Temperature dependent susceptibility might compromise the local magnetic field B_0 and the surrounding macroscopic field B_{mac} (43). This is a major drawback of the PRF method for accurate MR thermometry in and around fatty tissues (43, 62). While the temperature dependent magnetic susceptibility of water based tissue is rather small with $d\chi_{water}/dT = 0.0016 \text{ ppm}/^{\circ}\text{C}$ (muscle tissue (42)) as compared to the changes in the electron screening constant, the susceptibility of fat $d\chi_{fat}/dT = 0.0039 - 0.0076 \text{ ppm}/^{\circ}\text{C}$ (breast fat (43)) is close to the proton electron screening of water (43) (Table I). High fat content tissue consequently hampers temperature reading accuracy. Simulations in breast tissue demonstrated a maximum error of -8.6°C for an absolute temperature change of $\Delta T = 30^{\circ}\text{C}$ in HIFU ablation (43). Assuming more realistic temperature dependent susceptibilities of fat (63), this would result in a standard deviation of $\sim 1^{\circ}\text{C}$ for a $\Delta T = 5^{\circ}\text{C}$ in an hyperthermia application.

The temperature error ε_T based on magnetic susceptibility can be estimated given the following equation (43):

$$\varepsilon_T = -\frac{1}{\alpha} \left(\frac{\Delta B_{mac}}{B_0 \Delta T} - \frac{2}{3} \frac{\Delta \chi}{\Delta T} \right) \quad (6)$$

together with published values of temperature dependent magnetic susceptibilities of tissue (Table I).

To mitigate this error, hybrid methods combining the PRF shift and other temperature dependent MR parameters like apparent diffusion coefficient (64) or T_1 (34, 65, 66) are investigated. Multi gradient echoes with variable flip angles allow using the magnitude information for T_1 mapping and temperature related T_1 changes in lipids and the phase information for PRF thermometry in aqueous tissue (65, 66). While such hybrid methods are potentially appealing, its propensity to B_1 changes as well as temperature dependent M_0 and T_2^* changes reduce T_1 mapping accuracy. The choice of echo time TE is furthermore a compromise between T_1 mapping accuracy (short TEs preferable) and PRF based MR thermometry ($TE=T_2^*$ for maximum $SNR_{\Delta\phi}$ (67)) (65). Adding a high-bandwidth multi-echo readout allows for some improvement in mean PRF precision up to $\pm 1.3^\circ\text{C}$ and T_1 precision of $\pm 3.5\%$ (34).

A recently proposed MR method based on intermolecular multiple quantum coherences is insensitive to macroscopic field changes (26). With this approach an average error of 0.6°C for relative temperature measurements and 1.7°C for absolute temperature measurements was achieved (29, 30). While its imaging speed and SNR limitations currently prevent rapid temperature monitoring in thermal ablation, its potential for MR thermometry in hyperthermia therapies of several minutes heating time is intriguing.

Perfusion

Perfusion based phase changes unrelated to temperature changes may be misinterpreted and might over- or underestimate measured temperatures (21, 49). As an example, the severe over- and underestimation of PRF readings due to perfusion changes in muscle and tumour tissue is demonstrated in Figure 1b. In general alterations in the concentration of oxygen, which in its pure form is paramagnetic and diamagnetic when bound to hemoglobin (oxyhemoglobin) affect the local static magnetic field (49, 68). The direction of perfusion influences these local field changes (69). Various MR techniques exist, that allow to measure perfusion using first pass bolus exogenous contrasts. This includes dynamic susceptibility

contrast-enhanced (DSC) or dynamic contrast-enhanced (DCE) perfusion weighted MRI. Endogenous contrast based perfusion MRI techniques involve arterial spin labelling techniques (70, 71) and intra-voxel incoherent motion approaches (72). If these corrections need to or can be employed depends on the thermal therapy with its boundary conditions on temporal resolution and expected perfusion changes in the region of interest.

Motion

The PRF method is a relative temperature measurement relying on phase difference calculations versus a reference measurement. Any intra-scan motion leading to misregistration with the reference phase image results in temperature errors. These errors might be caused by respiratory, cardiac, peristaltic or bulk motion with standard deviations of $>\pm 10^{\circ}\text{C}$ even without any application of heat (25, 73). Structural changes of the treatment area due to tissue coagulation during an ablation procedure (40) can as well be misinterpreted as temperature changes. Thermal therapy duration typically exceeds clinical acceptable breathhold times of 10-20s or the duration of a cardiac cycle (~60 beats per minute), necessitating respiratory/cardiac gated temperature mapping (74, 75) or the use of navigator echoes for motion correction (76). The so called multi-baseline methods acquire not only one but a whole library of reference images during the respiratory/cardiac cycle. This library is used to link the phase measured during thermal therapy to the correct reference image by means of an acquired navigator echo (22), non-similarity coefficients (77) or intercorrelation coefficients (78, 79). While robust to periodic motion, reference or baseline methods are prone to irregular physiological motion such as arrhythmia.

Global magnetic field changes due to motion induced B_0 -drift or local magnetic field changes due to magnetic susceptibilities constitute another source for errors. Addressing the issue of irregular physiological motion is the forte of referenceless PRF methods which eliminate the use of a temporal reference via estimation of the background phase (23). Based on a region unaffected by thermal changes or a region unaffected by a thermal phase shift (fat) around the region of interest for thermal monitoring, the background phase information is fitted by a polynomial function (23, 49, 80, 81). Using a reweighted regression

even regions affected by thermal changes can be used to estimate the background phase (82). Since referenceless methods alone are sensitive to phase variations at organ interfaces due to susceptibility changes, combined referenceless multi-baseline methods have been suggested improving robustness (83). In addition, these methods hold the promise to track motion like organ deformation using intrinsic vasculature as landmarks (84). Referenceless methods have been successfully applied in vivo (85, 86).

Implants

A source of strong susceptibility artefacts and even signal voids are electrically conductive implants including stents, clips, sleeves, small osteosynthetic components etc, which are no contraindication for RF-hyperthermia, but disturb MRI. Even if the targeted region for the thermal therapy treatment is located sufficiently far away from these artefacts, near-implant temperature measurements might nevertheless be crucial for safety assessment. For the high powers applied in RF hyperthermia treatment significant temperature elevations can occur around electrically conductive implants due to electromagnetic induction. To avoid tissue damage these temperature elevations can be estimated using a fast analytical approach which has been demonstrated for coronary stents and which can be easily incorporated in hyperthermia treatment planning software (87). However for the majority of implants available, these generalized and rapid estimations are still missing, rendering online MR thermometry of near-implant temperatures necessary. Figure 2a, which displays magnitude and phase images acquired in and around an electrically conductive coronary stent at 7.0T, exemplifies the difficulties determining reliable temperature maps. The increasing number of phase wraps at prolonged TE for a constant spatial resolution reduces the range of sampled phase values and increases the risk of voxel misregistration, all of which reduces the fidelity of PRF MR thermometry. Even at shorter echo times, the calculated temperature maps display artefacts inside the stent as well as in regions in close vicinity to the stent. These artefacts are less pronounced in an imaging plane positioned few millimetres away from the stent (Figure 2b). This makes the evaluation of very local temperature challenging. However with prior knowledge of the expected EM induction effects and thermal distributions, accuracies of MR

thermometry using the PRF method correlate fairly well ($\sim 1^{\circ}\text{C}$) with fiber optic temperature probes (Figure 2c) (87, 88). Unlike the PRF method, T_1 based MR thermometry methods avoid the strong sensitivity towards susceptibility differences and hence provide superior fidelity ($< 1^{\circ}\text{C}$) over PRF if benchmarked against fiber optic temperature measurements (33, 89, 90).

Implications of thermal therapy hardware

The choice of hardware to induce temperature changes in tissue has significant implications on the feasibility, accuracy and/or spatial and temporal resolution of MR thermometry. In this chapter implications of invasive and non-invasive devices utilized for thermal therapies are discussed.

Interstitial devices

For interstitial and endocavitary hyperthermia treatments or ablation, devices are implanted in the target region e.g. within the tumor. Typically microwave or RF antennas, US transducers or laser fibers are utilized (91, 92). While laser fibers are relatively artefact free, RF ablative devices disturb the static magnetic field B_0 and cause susceptibility artefacts along with transmission and reception field perturbations making accurate thermal dose assessment in close vicinity to the device elusive. PRF based methods can provide a qualitative heating assessment around metal, however fail to provide accurate quantitative temperature data (93). Here T_1 based temperature mapping is more promising but still suffers from tradeoffs in speed and accuracy (33, 94). Imaging methods exist, that correct for slice-selection and frequency encoding distortions like slice encoding for metal artifact correction (SEMAC) (95) or multi-acquisition variable-resonance image combination (MAVRIC) (96). Yet, translation towards reasonable spatio-temporally resolved temperature maps is challenging. In general interstitial devices need to be investigated for possible MR imaging artefacts, which might falsify MR thermometry results.

MR guided hybrid systems

Various non-invasive ablation and hyperthermia methods exist, which are free of the aforementioned challenges for monitoring of interstitial devices. Magnetic resonance guided focused ultrasound (MRgFUS or MRgHIFU) utilizes acoustic energy directed at the target region (97). While MRI is a valuable tool for treatment planning, since cancerous tissue can be visualized, it is furthermore used to guide the ultrasound beam in conjunction with adjusting

the power levels by means of MR thermometry. In this procedure birdcage RF coils or large volume body RF coils are commonly used for signal transmission and reception for PRF or T_1 mapping based MR thermometry (97). Temperature mapping accuracy is a tradeoff between spatial and temporal resolution and highly dependent on the signal-to-noise ratio (SNR) available either for the MR thermometry method itself or for additional correction methods (B_1 mapping, perfusion measurements etc.). Local multichannel receive RF coils can enhance SNR significantly (98), which can be used for high spatial resolution MRI or parallel imaging techniques that accelerate image acquisition (99-102). While these multi-channel receive RF coils are clinical practice in diagnostic MRI applications, integration in a MRgFUS treatment device is challenging due to possible interferences of the ultrasound beam and the metallic/conducting structures of the RF coil array. To relax this issue customized phased array RF coils can be applied, which improve SNR as well as image acquisition speed (103). The construction of these arrays however is a compromise in RF coil design. The conductive path of the RF coil elements needs to be built "around" the ultrasound transducers or positioned behind the water bath required for coupling of the acoustic energy, preventing higher SNR to be achieved (103).

A similar challenge to gain highest possible SNR and parallel imaging performance for high spatial and temporal resolution MR temperature mapping is present in hybrid regional RF hyperthermia systems (Figure 3). These systems utilize electromagnetic fields in the radiofrequency range in order to focus power absorption to the target region (1, 24, 104-107). Here the same problem arises with an integration of multichannel receive arrays. The electrically conductive paths of the receive coils positioned closely to the body may influence the E-field distribution produced by the RF applicator for targeted hyperthermia. Other challenges are space constraints due to the magnet bore size and coupling of the RF hyperthermia hardware typically driven at high signal amplitudes ($>100V$) in continuous wave transmission while the receive architecture is designed to handle NMR signals in the range of $10^{-6}V$ (108). The latter is a potential source of imaging artefacts which needs to be addressed by additional filters or pre-amplifier design integrated in the hardware architecture of the MR system (Figure 3) (108). These errors may also be attributed to the hyperthermia treatment

frequency (100MHz) being rather close to the MR transmission frequency (64MHz), while other approaches using higher transmission frequencies (434MHz) didn't observe imaging artifacts. It should be noted that the latter setups used lower power levels (2x270W@434MHz (109) as compared to 900-1600W@100MHz (108)). Since image artifacts depend strongly on both transmitting and receiving RF hardware, it is therefore crucial to investigate and eliminate possible interferences in order to acquire reliable temperature information.

Integrated systems or thermal MR

Another approach for improved MR thermometry, which is currently under development, is an integrated system designated as thermal MR using the power amplifier and RF antennas for both MRI and targeted RF hyperthermia (31) (Figure 3). This is in particular attractive at ultra-high magnetic fields ($B_0 \geq 7.0\text{T}$, $f \geq 298\text{MHz}$), where multi-channel transmit hardware technology is available. Today, even clinical high field ($B_0 = 3.0\text{T}$, $f = 128\text{MHz}$) scanners are empowered with the ability to modify amplitude and phase of up to eight independent RF power amplifiers (110). In contrast to RF hyperthermia using continuous wave (CW) transmission, MR power amplifiers are designed to provide narrow band high peak power pulses. The average delivered power is determined by the RF pulse shape together with the applied repetition time and limited by the duty cycle and long term stability of the RFPA. At 7.0T with an integrated 8x1kW RFPA and ~30% RF cable losses to the RF coil plug, this would result in an average power of 560 W at a duty cycle of 10% (31). While UHF-MR systems equipped with 8x2kW or even 16x2kW are expected to become available soon, this would allow for an average RF power of 1120 W and 2240 W respectively, assuming similar duty cycle and RF losses. The advantage of a pulsed RFPA used for RF hyperthermia application and MR thermometry is the ability to modify the imaging technique in order to perform RF hyperthermia and MRI simultaneously at the same frequency. This approach exhibits the merit of an artefact free operation without the need for additional hardware modifications (31). In order to reach sufficient RF power deposition levels in tissue high power RF pulses used for imaging can be applied, off-resonance pulses can be incorporated in the imaging technique or a combination of the two. The advantage of using UHF-MR for temperature

monitoring is yet to be investigated and benchmarked against lower field systems. In addition to SNR gains and phase noise reduction at UHF (111-113), improvements are expected by using local multi-channel receive arrays for MR thermometry which demonstrated major SNR benefits over the use of the traditional RF body coil approach and are clinical routine ($B_0 \leq 3.0T$) (98, 114-116).

Ideal surface current pattern simulations that resemble RF receivers demonstrated, that curl-free components dominate at 7.0T as compared to divergence-free components that dominate at lower fields (117, 118). This justifies the use of birdcage type RF coils for transmission and loop RF coils for reception at lower fields ($B_0 \leq 3.0T$), while dipole antennas are well suited as transmit/receive elements for UHF MRI at $B_0 \geq 7.0T$ (31, 119-121) and above (122). SNR maps (123, 124) of a 16-channel bow tie dipole antenna array (121) and a 32-channel loop RF coil array (125) tailored for cardiac imaging at 7.0T emphasize this, showing higher SNR values acquired with a dipole antenna array versus the loop coil array (Figure 4) (121). The usage of dipole or "dipole-like" antennas as a targeted RF heating device is very well recognized by the hyperthermia community (104, 126-128). Recent reports demonstrated for the first time the feasibility of an integrated device that supports diagnostic MR, MR thermometry and localized RF hyperthermia using bow tie electric dipoles immersed in high permittivity dielectric (31). In addition to the discussed potential SNR gains for MR thermometry, the use of a higher RF hyperthermia frequency ($f=298MHz$) as compared to current clinically applied regional hyperthermia frequencies ($f=70-100MHz$) helps to create a smaller temperature hotspot. For body applications this allows to reduce the relevant temperature monitoring volume. This approach helps to preserve imaging time, reduce magnetic susceptibility artefacts created by heating of unwanted tissue regions or to use referenceless PRF methods typically applied for HIFU treatment (81). On the contrary regional RF hyperthermia could be as well performed in an integrated system at 3.0T with a proton resonance frequency of 128MHz. Current 3.0T MR systems are equipped with 32kW peak power amplifiers, driven at 10% duty cycle this would allow for 3.2kW average power which is double the value used in current hybrid systems with 1.6kW (108). Some research 3.0T scanners are even equipped with a multi-channel transmission system allowing for 8x8kW

(110). However MR imaging performance of electric dipole antennas at 3.0T still needs to be investigated.

Clinical studies

PRF thermometry has been applied successfully in clinical thermal therapies ranging from mild-hyperthermia treatment to thermal ablation. In MRgFUS treatment of uterine fibroids PRF thermometry is an important marker to adjust sonication power to ensure coagulation at the target and to monitor thermal dose (129, 130). In breast cancer treatment, using the PRF method alone evoked difficulties in the localization of the thermal hotspot due to fat regions (131). Here hybrid methods using additional T_1 contrast for temperature readings in fat reduced the PRF error significantly (34). Treating liver cancer with MRgFUS is hindered by the ribcage interfering with an efficient focusing of the acoustic energy and respiratory motion. To counter motion artefacts in PRF thermometry of the liver, respiratory gating, breathing control or fast 2D spoiled gradient echo sequences with acquisition times of ~ 3 s and spatial resolutions at ~ 1 mm (132-134) were employed. While these clinical reports are promising, more validation studies are essential to benchmark MR temperature reading accuracy against reference measurements derived from fiber optic temperature probes (Figure 1b). This research strives to eventually predict accurate necrosed tumor volumes based on thermal dose calculations.

MR guided RF hyperthermia on the other hand has been used successfully to treat human high grade sarcoma of the extremities or pelvis (105, 106, 135) and recurrent rectal carcinoma (49). Lengthy treatment times of >1 h evoked magnetic field drifts which were corrected by using external probes, the water bolus surrounding the patient or anatomical fat references with polynomial background phase fitting (46, 49, 106, 135). With this correction in place the standard deviation of PRF thermometry to fiber optic measurements was found to be $\sim 1^\circ\text{C}$ (Figure 1b). Temporal resolution constraints are more relaxed for RF hyperthermia treatments where tissue temperatures $\Delta T < 10^\circ\text{C}$ are applied for several minutes in contrast to MRgFUS ablation with temperatures $\Delta T > 30^\circ\text{C}$ reached in several seconds. On the other hand perfusion effects and their influence on temperature readings are pronounced in RF hyperthermia treatment in particular at treatment frequencies of 100Mhz or less due to an overall high volume of temperature increase and the associated thermoregulation. An

increase in perfusion and consequently diamagnetic oxyhemoglobin reduces the PRF and overestimates temperatures (Figure 1b) (49), which needs to be corrected.

Conclusions

This review aims at encouraging pioneers and early adopters interested in pursuing MR thermometry in basic and clinical research. Multiple clinical studies demonstrated the maturity of MR thermometry for in vivo applications (49, 106, 129, 130). The sensitivity of the PRF method to motion, perfusion and susceptibility changes, as well as the inability to measure temperatures in fatty tissue, are remaining challenges to improve accuracy and expand its clinical potential. Here promising solutions have been provided during the last years that overcome many of these obstacles and have been applied successfully in vivo (25, 34, 65, 66). The clinical application will ultimately dictate the MR methodologies used to monitor thermal therapies. While the time window for thermal ablations requires real-time monitoring, hyperthermia treatments with rather long treatment durations and smaller temperature increases are less constrained on the image acquisition side. New hardware solutions, in particular integrated MR systems at ultrahigh fields to control and monitor RF induced heating are promising to fully exploit the merits of state-of-the-art MR thermometry (31). The need for accurate MR thermometry will likely pave the way for further advances in MR methodology, MR technology and MR systems design with the ultimate goal of quantitative temperature mapping (25-28). The access to reliable temperature information will have major implications on basic and clinical research: enhancing the efficiency of thermal therapies, enabling better understanding of temperature related biological processes, boosting targeted drug delivery (136) and heat activated gene therapy monitoring (137) or improving safety and diagnostic capabilities of MRI applications while providing more realistic power limitations (138, 139).

Competing interests

Thoralf Niendorf is founder and CEO of MRI.TOOLS GmbH, Berlin, Germany.

Figure & Table Captions

Table I: Overview of relevant parameters for temperature error estimations: static magnetic field B_0 , chemical shift δ , permittivity ε , electric conductivity σ_{el} , permeability μ and magnetic volume susceptibility χ . The time dependent changes in B_0 are based on a magnetic field drift of the magnet over time. Electromagnetic property $(\varepsilon, \sigma, \mu)$ changes with temperature influence phase velocity of the RF pulse, B_1 and RF coil loading introducing additional echo time dependent phase changes. Please note that magnetic susceptibility might change as well due to perfusion and diffusion changes.

Figure 1: a-c) Clinical example of MR guided ($B_0 = 1.5$ T) RF hyperthermia treatment of recurrent rectal carcinoma. a) T1-weighted anatomical reference. b) Uncorrected temperature distribution together with the contours delineating anatomical fat regions used for phase drift correction. c) Corrected temperature distribution together with the contours delineating the tumor. For PRF thermometry spoiled gradient echo images were acquired after an RF heating duration of 57 minutes and temperature was calculated with regards to a reference phase map prior to the thermal therapy (49). d-f) Influence of perfusion changes on PRF thermometry in comparison to fiber optic temperature sensor readings in RF hyperthermia treatment of soft tissue sarcoma of the lower extremities. d) T1-weighted anatomical reference and location of the fiber optic temperature reading track. e) PRF thermometry showing the temperature hotspot. For PRF thermometry drift corrected phase difference of spoiled gradient echo images towards a reference prior to the thermal treatment was evaluated (106). f) Comparison of PRF thermometry and fiber optic thermometry. Sincere under- and overestimation in PRF thermometry in the presence of perfusion decrease and increase can be seen. In the muscle reactive perfusion increases during RF hyperthermia (on the left side away from the tip). In tumours no or low reactive perfusion is expected, showing very good accuracy ($<1^\circ\text{C}$) between fiber optic measurements and PRF thermometry. At the tumor margin perfusion declines (at the tip of the catheter), probably caused by the adjacent hyperperfused muscle (steal effect).

Figure 2: a) Echo time dependent magnitude and phase images at 7.0T of a coronary stent placed in an agar phantom. Please note how signal voids and phase wraps evolve with prolonged echo times. b) MR photograph of a coronary stent (left) used in RF heating experiments. PRF thermometry through the plane of the stent (middle) and in the plane slightly above the stent (right) using a double echo method (TE_1 and TE_2), where imaging artefacts are reduced. c) Comparison of MR thermometry and fiber optic thermometry in regions of the stent and surface regions of a homogeneous phantom (87).

Figure 3: Schematic of a hybrid MR guided RF hyperthermia system (1) and an integrated system presented recently (31). While the hybrid system requires two separate RF amplifiers and control units plus additional hardware filters that need to be incorporated into the standard MR hardware, the integrated system utilizes the proton excitation frequency of the MR system as well as its pulsed power amplifier and control unit to perform RF induced heating. Only transmit receive switches are added to the integrated system, which can be done externally as an integral part of the applicator and does not involve changes in the standard MR architecture itself (31).

Figure 4: SNR comparison of a 16-channel bow tie dipole array (121) and a 32-channel loop coil array (125) for cardiac imaging at 7.0 T. A 2D CiNE FLASH of a short axis view (SAX) ($1.1 \times 1.1 \times 2.5$ mm²) and its corresponding SNR map (123, 124) is displayed for a GRAPPA reduction factor $R=2$. The 16-channel bow tie dipole array shows higher mean SNR values as compared to the 32-channel loop coil indicating its feasibility for MRI at UHF ($B_0 = 7.0$ T) (121). The excellent image quality obtained from using dipole antennas for MRI demonstrates the rationale of these elements to be used for an integrated system.

References

1. Wust P, Hildebrandt B, Sreenivasa G, Rau B, Gellermann J, Riess H, et al. Hyperthermia in combined treatment of cancer. *Lancet Oncol*. 2002;3(8):487-97.
2. Kickhefel A, Weiss C, Roland J, Gross P, Schick F, Salomir R. Correction of susceptibility-induced GRE phase shift for accurate PRFS thermometry proximal to cryoablation iceball. *MAGMA*. 2012;25(1):23-31.
3. Focused Ultrasound Foundation; www.fusfoundation.org. 2015 [cited 2015 17.08.2015].
4. Tempany CMC, McDannold NJ, Hynynen K, Jolesz FA. Focused Ultrasound Surgery in Oncology: Overview and Principles. *Radiology*. 2011;259(1):39-56.
5. Jolesz FA, McDannold NJ. MRI-Guided Focused Ultrasound. *Intraoperative Imaging and Image-Guided Therapy*; Springer; 2014. p. 403-12.
6. Ghanouni P, Pauly KB, Elias WJ, Henderson J, Sheehan J, Monteith S, et al. Transcranial MRI-Guided Focused Ultrasound: A Review of the Technologic and Neurologic Applications. *Am J Roentgenol*. 2015;205(1):150-9.
7. Issels RD, Lindner LH, Verweij J, Wust P, Reichardt P, Schem BC, et al. Neo-adjuvant chemotherapy alone or with regional hyperthermia for localised high-risk soft-tissue sarcoma: A randomised phase 3 multicentre study. *Lancet Oncol*. 2010;11(6):561-70.
8. Oleson JR, Dewhirst MW, Harrelson JM, Leopold KA, Samulski TV, Tso CY. Tumor temperature distributions predict hyperthermia effect. *Int J Radiat Oncol Biol Phys*. 1989;16(3):559-70.
9. Issels RD, Prenninger SW, Nagele A, Boehm E, Sauer H, Jauch KW, et al. Ifosfamide plus etoposide combined with regional hyperthermia in patients with locally advanced sarcomas: a phase II study. *J Clin Oncol*. 1990;8(11):1818-29.
10. Leopold KA, Dewhirst MW, Samulski TV, Dodge RK, George SL, Blivin JL, et al. Cumulative minutes with T90 greater than tempindex is predictive of response of superficial malignancies to hyperthermia and radiation. *Int J Radiat Oncol Biol Phys*. 1993;25(5):841-7.
11. Hildebrandt B, Wust P, Ahlers O, Dieing A, Sreenivasa G, Kerner T, et al. The cellular and molecular basis of hyperthermia. *Crit Rev Oncol Hematol*. 2002;43(1):33-56.
12. van der Zee M.D PDJ, Peer-Valstar M.D JN, Rietveld M.Sc PJM, de Graaf-Strukowska M.D L, van Rhooon Ph.D GC. Practical Limitations of Interstitial Thermometry During Deep Hyperthermia. *Int J Radiat Oncol Biol Phys*. 1998;40(5):1205-12.
13. W. Tilly PW, B. Rau, C. Harder, J. Gellermann, P. Schlag, V. Budach, R. Felix. Temperature data and specific absorption rates in pelvic tumours: predictive factors and correlations. *Int J Hyperthermia*. 2001;17(2):172-88.
14. Rau B, Wust P, Tilly W, Gellermann J, Harder C, Riess H, et al. Preoperative radiochemotherapy in locally advanced or recurrent rectal cancer: regional radiofrequency hyperthermia correlates with clinical parameters. *Int J Radiat Oncol Biol Phys*. 2000;48(2):381-91.
15. Tilly W, Gellermann J, Graf R, Hildebrandt B, Weißbach L, Budach V, et al. Regional Hyperthermia in Conjunction with Definitive Radiotherapy against Recurrent or Locally Advanced Prostate Cancer T3 pN0 M0. *Strahlenther Onkol*. 2005;181(1):35-41.
16. van Rhooon GC, Wust P. Introduction: Non-invasive thermometry for thermotherapy. *Int J Hyperthermia*. 2005;21(6):489-95.
17. Le Bihan D, Delannoy J, Levin RL. Temperature mapping with MR imaging of molecular diffusion: application to hyperthermia. *Radiology*. 1989;171(3):853-7.

18. Dewhirst MW, Sostman HD, Leopold KA, Charles H, Moore D, Burn R, et al. Soft-tissue sarcomas: MR imaging and MR spectroscopy for prognosis and therapy monitoring. *Work in progress. Radiology.* 1990;174(3):847-53.
19. De Poorter J, De Wagter C, De Deene Y, Thomsen C, Stahlberg F, Achten E. The proton-resonance-frequency-shift method compared with molecular diffusion for quantitative measurement of two-dimensional time-dependent temperature distribution in a phantom. *Journal of Magnetic Resonance, Series B.* 1994;103(3):234-41.
20. Ishihara Y, Calderon A, Watanabe H, Okamoto K, Suzuki Y, Kuroda K. A precise and fast temperature mapping using water proton chemical shift. *Magn Reson Med.* 1995;34(6):814-23.
21. De Poorter JD, De Wagter CD, De Deene YD, Thomsen C, Ståhlberg F, Achten E. Noninvasive MRI thermometry with the proton resonance frequency (PRF) method: in vivo results in human muscle. *Magn Reson Med.* 1995;33(1):74-81.
22. Vigen K, Daniel B, Pauly J, Butts K. Triggered, navigated, multi-baseline method for proton resonance frequency temperature mapping with respiratory motion. *Magn Reson Med.* 2003;50(5):1003-10.
23. Rieke V, Vigen K, Sommer G, Daniel B, Pauly J, Butts K. Referenceless PRF shift thermometry. *Magn Reson Med.* 2004;51(6):1223-31.
24. Gellermann J, Wlodarczyk W, Feussner A, Föhling H, Nadobny J, Hildebrandt B, et al. Methods and potentials of magnetic resonance imaging for monitoring radiofrequency hyperthermia in a hybrid system. *Int J Hyperthermia.* 2005;21(6):497-513.
25. Grissom WA, Rieke V, Holbrook AB, Medan Y, Lustig M, Santos J, et al. Hybrid referenceless and multibaseline subtraction MR thermometry for monitoring thermal therapies in moving organs. *Med Phys.* 2010;37:5014.
26. Galiana G, Branca RT, Jenista ER, Warren WS. Accurate temperature imaging based on intermolecular coherences in magnetic resonance. *Science.* 2008;322(5900):421-4.
27. Sprinkhuizen SM, Bakker CJG, Bartels LW. Absolute MR thermometry using time-domain analysis of multi-gradient-echo magnitude images. *Magn Reson Med.* 2010;64(1):239-48.
28. Streicher MN, Schäfer A, Ivanov D, Müller DK, Amadon A, Reimer E, et al. Fast accurate MR thermometry using phase referenced asymmetric spin-echo EPI at high field. *Magn Reson Med.* 2014;71(2):524-33.
29. Davis RM, Warren WS. Intermolecular zero quantum coherences enable accurate temperature imaging in red bone marrow. *Magn Reson Med.* 2014;[Epub ahead of print].
30. Davis RM, Zhou Z, Chung H, Warren WS. Multi-spin echo spatial encoding provides three-fold improvement of temperature precision during intermolecular zero quantum thermometry. *Magn Reson Med.* 2015;[Epub ahead of print].
31. Winter L, Özerdem C, Hoffmann W, Santoro D, Müller A, Waiczies H, et al. Design and Evaluation of a Hybrid Radiofrequency Applicator for Magnetic Resonance Imaging and RF Induced Hyperthermia: Electromagnetic Field Simulations up to 14.0 Tesla and Proof-of-Concept at 7.0 Tesla. *PLOS ONE.* 2013;8(4):e61661.
32. Chen J, Daniel BL, Pauly KB. Investigation of proton density for measuring tissue temperature. *J Magn Reson Imaging.* 2006;23(3):430-4.
33. Gensler D, Fidler F, Ehses P, Warmuth M, Reiter T, Duering M, et al. MR safety: Fast T1 thermometry of the RF-induced heating of medical devices. *Magn Reson Med.* 2012;68(5):1593-9.
34. Todd N, Diakite M, Payne A, Parker DL. In vivo evaluation of multi-echo hybrid PRF/T1 approach for temperature monitoring during breast MR-guided focused ultrasound surgery treatments. *Magn Reson Med.* 2014;72(3):793-9.

35. Graham SJ, Bronskill MJ, Henkelman RM. Time and temperature dependence of MR parameters during thermal coagulation of ex vivo rabbit muscle. *Magn Reson Med*. 1998;39(2):198-203.
36. Baron P, Ries M, Deckers R, Greef M, Tanttu J, Köhler M, et al. In vivo T2-based MR thermometry in adipose tissue layers for high-intensity focused ultrasound near-field monitoring. *Magn Reson Med*. 2014;72(4):1057-64.
37. Samulski T, MacFall J, Zhang Y, Grant W, Charles C. Non-invasive thermometry using magnetic resonance diffusion imaging: potential for application in hyperthermic oncology. *Int J Hyperthermia*. 1992;8(6):819-29.
38. MacFall J, Prescott D, Fullar E, Samulski T. Temperature dependence of canine brain tissue diffusion coefficient measured in vivo with magnetic resonance echo-planar imaging. *Int J Hyperthermia*. 1995;11(1):73-86.
39. Graham S, Stanisz G, Kecojevic A, Bronskill M, Henkelman R. Analysis of changes in MR properties of tissues after heat treatment. *Magn Reson Med*. 1999;42(6):1061-71.
40. Rieke V, Pauly K. MR thermometry. *J Magn Reson Med*. 2008;27(2):376-90.
41. Hindman J. Proton resonance shift of water in the gas and liquid states. *J Chem Phys*. 1966;44:4582.
42. De Poorter J. Noninvasive MRI thermometry with the proton resonance frequency method: study of susceptibility effects. *Magn Reson Med*. 1995;34(3):359-67.
43. Sprinkhuizen SM, Konings MK, van der Bom MJ, Viergever MA, Bakker CJ, Bartels LW. Temperature-induced tissue susceptibility changes lead to significant temperature errors in PRFS-based MR thermometry during thermal interventions. *Magn Reson Med*. 2010;64(5):1360-72.
44. Peters RT, Hinks RS, Henkelman RM. Ex vivo tissue-type independence in proton-resonance frequency shift MR thermometry. *Magn Reson Med*. 1998;40(3):454-9.
45. McDannold N. Quantitative MRI-based temperature mapping based on the proton resonant frequency shift: review of validation studies. *Int J Hyperthermia*. 2005;21(6):533-46.
46. Gellermann J, Wlodarczyk W, Ganter H, Nadobny J, Föhling H, Seebass M, et al. A practical approach to thermography in a hyperthermia/magnetic resonance hybrid system: Validation in a heterogeneous phantom. *Int J Radiat Oncol Biol Phys*. 2005;61(1):267-77.
47. Kuroda K, Oshio K, Chung AH, Hynynen K, Jolesz FA. Temperature mapping using the water proton chemical shift: a chemical shift selective phase mapping method. *Magn Reson Med*. 1997;38(5):845-51.
48. Martin E, Jeanmonod D, Morel A, Zadicario E, Werner B. High-intensity focused ultrasound for noninvasive functional neurosurgery. *Ann Neurol*. 2009;66(6):858-61.
49. Gellermann J, Wlodarczyk W, Hildebrandt B, Ganter H, Nicolau A, Rau B, et al. Noninvasive magnetic resonance thermography of recurrent rectal carcinoma in a 1.5 Tesla hybrid system. *Cancer Res* 2005;65(13):5872-80.
50. Tarasek MR, Pellicer R, Hofstetter LW, Numan WC, Bakker JF, Kotek G, et al. Validation of MR thermometry: Method for temperature probe sensor registration accuracy in head and neck phantoms. *Int J Hyperthermia*. 2014;30(2):142-9.
51. Stollberger R, Ascher PW, Huber D, Renhart W, Radner H, Ebner F. Invited. Temperature monitoring of interstitial thermal tissue coagulation using MR phase images. *J Magn Reson Imaging*. 1998;8(1):188-96.
52. Dixon WT. Simple proton spectroscopic imaging. *Radiology*. 1984;153(1):189-94.
53. Soher BJ, Wyatt C, Reeder SB, MacFall JR. Noninvasive temperature mapping with MRI using chemical shift water-fat separation. *Magn Reson Med*. 2010;63(5):1238-46.

54. Fleckenstein J, Archer B, Barker B, Vaughan J, Parkey R, Peshock R. Fast short-tau inversion-recovery MR imaging. *Radiology*. 1991;179(2):499-504.
55. Yuan J, Mei C-S, Panych LP, McDannold NJ, Madore B. Towards fast and accurate temperature mapping with proton resonance frequency-based MR thermometry. *Quant Imaging Med Surg*. 2012;2(1):21.
56. Meyer C, Pauly J, Macovski A, Nishimura D. Simultaneous spatial and spectral selective excitation. *Magn Reson Med*. 1990;15(2):287-304.
57. Weidensteiner C, Quesson B, Caire-Gana B, Keroui N, Rullier A, Trillaud H, et al. Real-time MR temperature mapping of rabbit liver in vivo during thermal ablation. *Magn Reson Med*. 2003;50(2):322-30.
58. Grissom W, Kerr A, Holbrook A, Pauly J, Butts-Pauly K. Maximum Linear-Phase Spectral-Spatial RF Pulses for Fat-Suppressed PRF-Shift MR Thermometry. *Magn Reson Med*. 2009;62(5):1242.
59. Yuan J, Mei C-S, Madore B, McDannold NJ, Panych LP. Fast fat-suppressed reduced field-of-view temperature mapping using 2DRF excitation pulses. *J Magn Reson*. 2011;210(1):38-43.
60. Peters RD, Henkelman RM. Proton-resonance frequency shift MR thermometry is affected by changes in the electrical conductivity of tissue. *Magn Reson Med*. 2000;43(1):62-71.
61. Stoy RD, Foster KR, Schwan HP. Dielectric properties of mammalian tissues from 0.1 to 100 MHz; a summary of recent data. *Phys Med Biol*. 1982;27(4):501.
62. Baron P, Deckers R, Bouwman JG, Bakker CJ, de Greef M, Viergever MA, et al. Influence of water and fat heterogeneity on fat-referenced MR thermometry. *Magn Reson Med*. 2015.
63. Sprinkhuizen SM, Bakker CJ, Ippel JH, Boelens R, Viergever MA, Bartels LW. Temperature dependence of the magnetic volume susceptibility of human breast fat tissue: an NMR study. *MAGMA*. 2012;25(1):33-9.
64. Das SK, Macfall J, McCauley R, Craciunescu O, Dewhirst MW, Samulski TV. Improved magnetic resonance thermal imaging by combining proton resonance frequency shift (PRFS) and apparent diffusion coefficient (ADC) data. *International Journal of Hyperthermia*. 2005;21(7):657-67.
65. Todd N, Diakite M, Payne A, Parker DL. Hybrid proton resonance frequency/T1 technique for simultaneous temperature monitoring in adipose and aqueous tissues. *Magn Reson Med*. 2013;69(1):62-70.
66. Baron P, Deckers R, Greef M, Merckel LG, Bakker CJ, Bouwman JG, et al. Correction of proton resonance frequency shift MR-thermometry errors caused by heat-induced magnetic susceptibility changes during high intensity focused ultrasound ablations in tissues containing fat. *Magn Reson Med*. 2014;72(6):1580-9.
67. Cline HE, Hynynen K, Schneider E, Hardy CJ, Maier SE, Watkins RD, et al. Simultaneous magnetic resonance phase and magnitude temperature maps in muscle. *Magnetic Resonance in Medicine*. 1996;35(3):309-15.
68. Streicher MN, Schäfer A, Reimer E, Dhital B, Trampel R, Ivanov D, et al. Effects of air susceptibility on proton resonance frequency MR thermometry. *MAGMA*. 2012;25(1):41-7.
69. Le Bihan D, Breton E, Lallemand D, Aubin M, Vignaud J, Laval-Jeantet M. Separation of diffusion and perfusion in intravoxel incoherent motion MR imaging. *Radiology*. 1988;168(2):497-505.
70. Detre JA, Wang J, Wang Z, Rao H. Arterial spin-labeled perfusion MRI in basic and clinical neuroscience. *Current opinion in neurology*. 2009;22(4):348-55.

71. Essig M, Shiroishi MS, Nguyen TB, Saake M, Provenzale JM, Enterline D, et al. Perfusion MRI: the five most frequently asked technical questions. *AJR American journal of roentgenology*. 2013;200(1):24.
72. Le Bihan D, Breton E, Lallemand D, Grenier P, Cabanis E, Laval-Jeantet M. MR imaging of intravoxel incoherent motions: application to diffusion and perfusion in neurologic disorders. *Radiology*. 1986;161(2):401-7.
73. Rieke V, Kinsey AM, Ross AB, Nau WH, Diederich CJ, Sommer G, et al. Referenceless MR thermometry for monitoring thermal ablation in the prostate. *IEEE Trans Med Imaging*. 2007;26(6):813-21.
74. Lepetit-Coiffé M, Quesson B, Seror O, Dumont E, Le Bail B, Moonen CT, et al. Real-time monitoring of radiofrequency ablation of rabbit liver by respiratory-gated quantitative temperature MRI. *J Magn Reson Imaging*. 2006;24(1):152-9.
75. Frauenrath T, Hezel F, Heinrichs U, Kozerke S, Utting J, Kob M, et al. Feasibility of cardiac gating free of interference with electro-magnetic fields at 1.5 Tesla, 3.0 Tesla and 7.0 Tesla using an MR-stethoscope. *Invest Radiol*. 2009;44(9):539-47.
76. de Zwart JA, Vimeux FC, Palussiere J, Salomir R, Quesson B, Delalande C, et al. On-line correction and visualization of motion during MRI-controlled hyperthermia. *Magn Reson Med*. 2001;45(1):128-37.
77. Shmatukha AV, Bakker CJ. Correction of proton resonance frequency shift temperature maps for magnetic field disturbances caused by breathing. *Phys Med Biol*. 2006;51(18):4689.
78. De Senneville BD, Mougnot C, Moonen CT. Real-time adaptive methods for treatment of mobile organs by MRI-controlled high-intensity focused ultrasound. *Magnetic Resonance in Medicine*. 2007;57(2):319-30.
79. Roujol S, Ries M, Quesson B, Moonen C, Denis de Senneville B. Real-time MR-thermometry and dosimetry for interventional guidance on abdominal organs. *Magnetic Resonance in Medicine*. 2010;63(4):1080-7.
80. Kuroda K, Kokuryo D, Kumamoto E, Suzuki K, Matsuoka Y, Keserci B. Optimization of self-reference thermometry using complex field estimation. *Magn Reson Med*. 2006;56(4):835-43.
81. Salomir R, Viallon M, Kickhefel A, Roland J, Morel DR, Petrusca L, et al. Reference-free PRFS MR-thermometry using near-harmonic 2-D reconstruction of the background phase. *IEEE Trans Med Imaging*. 2012;31(2):287-301.
82. Grissom W, Lustig M, Holbrook A, Rieke V, Pauly J, Butts-Pauly K. Reweighted 11 Referenceless PRF Shift Thermometry. *Magn Reson Med*. 2010;64(4):1068-77.
83. Grissom W, Rieke V, Santos J, Swaminathan A, Pauly J, Pauly K, et al. Hybrid referenceless and multi-baseline subtraction thermometry for monitoring thermal therapies in the heart. *Journal of Cardiovascular Magnetic Resonance*. 2010;12(Suppl 1):P62.
84. Madore B, Panych LP, Mei CS, Yuan J, Chu R. Multipathway sequences for MR thermometry. *Magn Reson Med*. 2011;66(3):658-68.
85. Kickhefel A, Rosenberg C, Roland J, Viallon M, Gross P, Schick F, et al. A pilot study for clinical feasibility of the near-harmonic 2D referenceless PRFS thermometry in liver under free breathing using MR-guided LITT ablation data. *Int J Hyperthermia*. 2012;28(3):250-66.
86. Holbrook AB, Ghanouni P, Santos JM, Dumoulin C, Medan Y, Pauly KB. Respiration based steering for high intensity focused ultrasound liver ablation. *Magn Reson Med*. 2014;71(2):797-806.
87. Winter L, Oberacker E, Özerdem C, Ji Y, von Knobelsdorff-Brenkenhoff F, Weidemann G, et al. On the RF heating of coronary stents at 7.0 Tesla MRI. *Magn Reson Med*. 2014;[Epub ahead of print].

88. Santoro D, Winter L, Müller A, Vogt J, Renz W, Özerdem C, et al. Detailing Radio Frequency Heating Induced by Coronary Stents: A 7.0 Tesla Magnetic Resonance Study. *PLOS ONE*. 2012;7(11):e49963.
89. Detti V, Grenier D, Perrin E, Beuf O. Assessment of radiofrequency self-heating around a metallic wire with MR T1-based thermometry. *Magn Reson Med*. 2011;66(2):448-55.
90. Weber H, Yoon D, Valentina T, Butts Pauly K, Hargreaves BA. T1-Based MR Thermometry Close to Metal. *Proc Intl Soc Mag Reson Med*. 2015.
91. Kickhefel A, Rosenberg C, Weiss CR, Rempp H, Roland J, Schick F, et al. Clinical evaluation of MR temperature monitoring of laser-induced thermotherapy in human liver using the proton-resonance-frequency method and predictive models of cell death. *J Magn Reson Imaging*. 2011;33(3):704-9.
92. de Senneville BD, Roujol S, Jaïs P, Moonen CTW, Herigault G, Quesson B. Feasibility of fast MR-thermometry during cardiac radiofrequency ablation. *NMR Biomed*. 2012;25(4):556-62.
93. Ehses P, Fidler F, Nordbeck P, Pracht ED, Warmuth M, Jakob PM, et al. MRI thermometry: Fast mapping of RF-induced heating along conductive wires. *Magn Reson Med*. 2008;60(2):457-61.
94. Deichmann R, Hahn D, Haase A. Fast T1 mapping on a whole-body scanner. *Magn Reson Med*. 1999;42(1):206-9.
95. Lu W, Pauly KB, Gold GE, Pauly JM, Hargreaves BA. SEMAC: slice encoding for metal artifact correction in MRI. *Magn Reson Med*. 2009;62(1):66-76.
96. Koch KM, Lorbiecki JE, Hinks RS, King KF. A multispectral three-dimensional acquisition technique for imaging near metal implants. *Magn Reson Med*. 2009;61(2):381-90.
97. Huber PE, Jenne JW, Rastert R, Simiantonakis I, Sinn H-P, Strittmatter H-J, et al. A new noninvasive approach in breast cancer therapy using magnetic resonance imaging-guided focused ultrasound surgery. *Cancer Res*. 2001;61(23):8441-7.
98. Roemer P, Edelstein W, Hayes C, Souza S, Mueller O. The NMR phased array. *Magn Reson Med*. 1990;16(2):192-225.
99. Sodickson DK, Manning WJ. Simultaneous acquisition of spatial harmonics (SMASH): fast imaging with radiofrequency coil arrays. *Magn Reson Med*. 1997;38(4):591-603.
100. Pruessmann KP, Weiger M, Scheidegger MB, Boesiger P. SENSE: sensitivity encoding for fast MRI. *Magn Reson Med*. 1999;42(5):952-62.
101. Griswold MA, Jakob PM, Heidemann RM, Nittka M, Jellus V, Wang J, et al. Generalized autocalibrating partially parallel acquisitions (GRAPPA). *Magn Reson Med*. 2002;47(6):1202-10.
102. Bankson J, Stafford R, Hazle J. Partially parallel imaging with phase-sensitive data: Increased temporal resolution for magnetic resonance temperature imaging. *Magn Reson Med*. 2005;53(3):658-65.
103. Minalga E, Payne A, Merrill R, Todd N, Vijayakumar S, Kholmovski E, et al. An 11-channel radio frequency phased array coil for magnetic resonance guided high-intensity focused ultrasound of the breast. *Magn Reson Med*. 2013;69(1):295-302.
104. Delannoy J, LeBihan D, Hoult D, Levin R. Hyperthermia system combined with a magnetic resonance imaging unit. *Med Phys*. 1990;17(5):855-60.
105. Carter DL, MacFall JR, Clegg ST, Wan X, Prescott DM, Charles HC, et al. Magnetic resonance thermometry during hyperthermia for human high-grade sarcoma. *Int J Radiat Oncol Biol Phys*. 1998;40(4):815.
106. Gellermann J, Hildebrandt B, Issels R, Ganter H, Wlodarczyk W, Budach V, et al. Noninvasive magnetic resonance thermography of soft tissue sarcomas during regional hyperthermia. *Cancer*. 2006;107(6):1373-82.

107. Paulides M, Bakker J, Hofstetter L, Numan W, Pellicer R, Fiveland E, et al. Laboratory prototype for experimental validation of MR-guided radiofrequency head and neck hyperthermia. *Phys Med Biol*. 2014;59(9):2139.
108. Gellermann J, Faehling H, Mielec M, Cho C, Budach V, Wust P. Image artifacts during MRT hybrid hyperthermia-Causes and elimination. *Int J Hyperthermia*. 2008;24(4):327-35.
109. Numan WC, Hofstetter LW, Kotek G, Bakker JF, Fiveland EW, Houston GC, et al. Exploration of MR-guided head and neck hyperthermia by phantom testing of a modified prototype applicator for use with proton resonance frequency shift thermometry. *Int J Hyperthermia*. 2014;30(3):184-91.
110. Waxmann P, Lindel T, Seifert F, Ittermann B, Mekle R. Improved off-resonance correction for segmented spatially selective excitation pulses to achieve large excitation bandwidth. *Proc Intl Soc Mag Reson Med*. 2013;4259.
111. Niendorf T, Sodickson DK, Krombach GA, Schulz-Menger J. Toward cardiovascular MRI at 7 T: clinical needs, technical solutions and research promises. *European radiology*. 2010;20(12):2806-16. Epub 2010/08/03.
112. Niendorf T, Graessl A, Thalhammer C, Dieringer MA, Kraus O, Santoro D, et al. Progress and promises of human cardiac magnetic resonance at ultrahigh fields: A physics perspective. *J Magn Reson*. 2012;229(0):208-22.
113. Niendorf T, Paul K, C O, Graessl A, Klix S, Huelnhagen T, et al. W(h)ither Human Cardiac and Body Magnetic Resonance at Ultrahigh Fields? Technical Advances, Practical Considerations, Applications, and Clinical Opportunities. *NMR Biomed*. 2015.
114. Niendorf T, Hardy CJ, Giaquinto RO, Gross P, Cline HE, Zhu Y, et al. Toward single breath-hold whole-heart coverage coronary MRA using highly accelerated parallel imaging with a 32-channel MR system. *Magn Reson Med*. 2006;56(1):167-76.
115. Schmitt M, Potthast A, Sosnovik DE, Polimeni JR, Wiggins GC, Triantafyllou C, et al. A 128-channel receive-only cardiac coil for highly accelerated cardiac MRI at 3 Tesla. *Magn Reson Med*. 2008;59(6):1431-9.
116. Winter L, Kellman P, Renz W, Gräbl A, Hezel F, Thalhammer C, et al. Comparison of three multichannel transmit/receive radiofrequency coil configurations for anatomic and functional cardiac MRI at 7.0T: implications for clinical imaging. *Eur Radiol*. 2012;22(10):2211-20. Epub 2012 Jun 1.
117. Schnell W. Rauschoptimierung von Oberflächen- und Ganzkörperantennen für die Kernspintomographie. Bochum: Ruhr-Universität Bochum; 1997.
118. Lattanzi R, Sodickson DK. Ideal current patterns yielding optimal signal-to-noise ratio and specific absorption rate in magnetic resonance imaging: Computational methods and physical insights. *Magn Reson Med*. 2012;68(1):286-304.
119. Raaijmakers A, Ipek O, Klomp D, Possanzini C, Harvey P, Lagendijk J, et al. Design of a radiative surface coil array element at 7 T: The single side adapted dipole antenna. *Magn Reson Med*. 2011;66(5):1488-97.
120. Raaijmakers AJ, Italiaander M, Voogt IJ, Lujten PR, Hoogduin JM, Klomp DW, et al. The fractionated dipole antenna: A new antenna for body imaging at 7 Tesla. *Magn Reson Med*. 2015;[Epub ahead of print].
121. Oezerdem C, Winter L, Graessl A, Paul K, Els A, Weinberger O, et al. 16 Channel Bow Tie Antenna Transceiver Array for Cardiac Magnetic Resonance at 7.0T. *Magn Reson Med*. 2015;[Epub ahead of print].
122. Winter L, Niendorf T. On the electrodynamic constraints and antenna array design for human in vivo MR up to 70 Tesla and EPR up to 3GHz. *Proc Intl Soc Mag Reson Med*. 2015.
123. Kellman P, McVeigh ER. Image reconstruction in SNR units: A general method for SNR measurement†. *Magn Reson Med*. 2005;54(6):1439-47.

124. Kellman P. Erratum to Kellman P, McVeigh ER. Image reconstruction in SNR units: a general method for SNR measurement. *Magn Reson Med*. 2005; 54: 1439–1447. *Magn Reson Med*. 2007;58(1):211-2.
125. Graessl A, Renz W, Hezel F, Dieringer M, Winter L, Oezerdem C, et al. Modular 32 Channel Transceiver Coil Array for Cardiac MRI at 7T. *Magn Reson Med*. 2014;72(1):276-90.
126. Wust P, Nadobny J, Felix R, Deulhard P, Louis A, John W. Strategies for optimized application of annular-phased-array systems in clinical hyperthermia. *Int J Hyperthermia*. 1991;7(1):157-73.
127. Wust P, Seebass M, Nadobny J, Deulhard P, Mönich G, Felix R. Simulation studies promote technological development of radiofrequency phased array hyperthermia. *Int J Hyperthermia*. 1996;12(4):477-94.
128. Paulides MM, Bakker JF, van Rhooen GC. Electromagnetic head-and-neck hyperthermia applicator: experimental phantom verification and FDTD model. *Int J Radiat Oncol Biol Phys*. 2007;68(2):612-20.
129. Tempny CM, Stewart EA, McDannold N, Quade BJ, Jolesz FA, Hynynen K. MR Imaging-guided Focused Ultrasound Surgery of Uterine Leiomyomas: A Feasibility Study 1. *Radiology*. 2003;226(3):897-905.
130. Kim HS, Baik J-H, Pham LD, Jacobs MA. MR-guided high-intensity focused ultrasound treatment for symptomatic uterine leiomyomata: long-term outcomes. *Acad Radiol*. 2011;18(8):970-6.
131. Gianfelice D, Khiat A, Amara M, Belblidia A, Boulanger Y. MR Imaging-guided Focused US Ablation of Breast Cancer: Histopathologic Assessment of Effectiveness—Initial Experience 1. *Radiology*. 2003;227(3):849-55.
132. Okada A, Murakami T, Mikami K, Onishi H, Tanigawa N, Marukawa T, et al. A case of hepatocellular carcinoma treated by MR-guided focused ultrasound ablation with respiratory gating. *Magn Reson Med Sci*. 2006;5(3):167-71.
133. Fischer K, Gedroyc W, Jolesz FA. Focused ultrasound as a local therapy for liver cancer. *Cancer J*. 2010;16(2):118-24.
134. Zaccagna F, Anzidei M, Sandolo F, Cavallo Marincola B, Palla C, Leonardi A, et al. MRgFUS for liver and pancreas cancer treatments: the Umberto I hospital experience. *Transl Cancer Res*. 2014;3(5):430-41.
135. Craciunescu OI, Stauffer PR, Soher BJ, Wyatt CR, Arabe O, Maccarini P, et al. Accuracy of real time noninvasive temperature measurements using magnetic resonance thermal imaging in patients treated for high grade extremity soft tissue sarcomas. *Med Phys*. 2009;36(11):4848-58.
136. McDaniel JR, Dewhirst MW, Chilkoti A. Actively targeting solid tumours with thermoresponsive drug delivery systems that respond to mild hyperthermia. *International Journal of Hyperthermia*. 2013(0):1-10.
137. Frenkel V. Ultrasound mediated delivery of drugs and genes to solid tumors. *Adv Drug Deliver Rev*. 2008;60(10):1193-208.
138. Murbach M, Neufeld E, Capstick M, Kainz W, Brunner DO, Samaras T, et al. Thermal Tissue Damage Model Analyzed for Different Whole-Body SAR and Scan Durations for Standard MR Body Coils. *Magn Reson Med*. 2013;71(1):421-31.
139. van Rhooen GC, Samaras T, Yarmolenko PS, Dewhirst MW, Neufeld E, Kuster N. CEM43° C thermal dose thresholds: a potential guide for magnetic resonance radiofrequency exposure levels? *European Radiology*. 2013:1-13.

Parameter		Value	
Static magnetic field	dB_0/dt	field drift	0.02 ppm/h (88)
Chemical shift	$d\delta/dT$	pure water	-0.01 ppm/°C (41)
		tissue (except fat)	-(0.009-0.01) ppm/°C (45)
		fat	-0.00018 ppm/°C (51)
Permittivity	$d\epsilon/dT$	water	-0.5 %/°C (60)
Electrical conductivity	$d\sigma_{el}/dT$	dog muscle	1.7 %/°C (61)
Permeability	$d\mu/dT$	water	$3 \cdot 10^{-7}$ %/°C (60)
Magnetic susceptibility	$d\chi/dT$	pure water	0.0026 ppm/°C (30-45°C) (42)
		muscle	0.0016 ppm/°C (30-45°C) (42)
		breast fat	0.0039-0.0076 ppm/°C (63)
		air	-0.002 ppm/°C (68)

Table I: Overview of relevant parameters for temperature error estimations: static magnetic field B_0 , chemical shift δ , permittivity ϵ , electric conductivity σ_{el} , permeability μ and magnetic volume susceptibility χ . The time dependent changes in B_0 are based on a magnetic field drift of the magnet over time. Electromagnetic property (ϵ, σ, μ) changes with temperature influence phase velocity of the RF pulse, B_1 and RF coil loading introducing additional echo time dependent phase changes. Please note that magnetic susceptibility might change as well due to perfusion and diffusion changes.

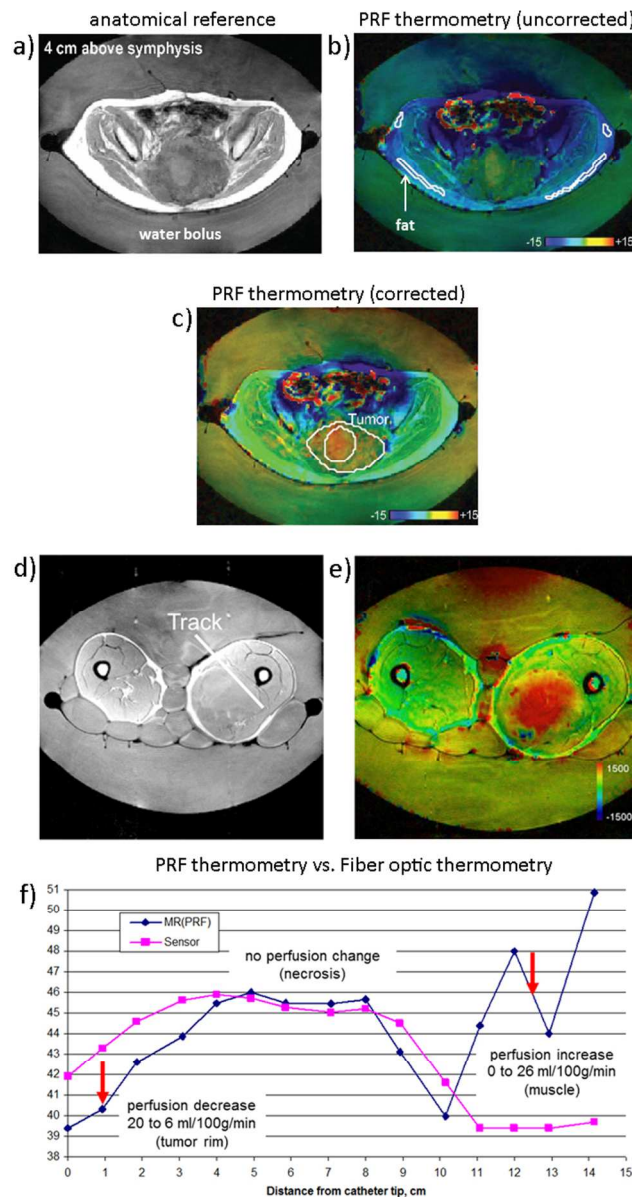


Figure 1: a-c) Clinical example of MR guided ($B_0 = 1.5$ T) RF hyperthermia treatment of recurrent rectal carcinoma. a) T1-weighted anatomical reference. b) Uncorrected temperature distribution together with the contours delineating anatomical fat regions used for phase drift correction. c) Corrected temperature distribution together with the contours delineating the tumor. For PRF thermometry spoiled gradient echo images were acquired after an RF heating duration of 57 minutes and temperature was calculated with regards to a reference phase map prior to the thermal therapy (48). d-f) Influence of perfusion changes on PRF thermometry in comparison to fiber optic temperature sensor readings in RF hyperthermia treatment of soft tissue sarcoma of the lower extremities. d) T1-weighted anatomical reference and location of the fiber optic temperature reading track. e) PRF thermometry showing the temperature hotspot. For PRF thermometry drift corrected phase difference of spoiled gradient echo images towards a reference prior to the thermal treatment was evaluated (105). f) Comparison of PRF thermometry and fiber optic thermometry. Sincere under- and overestimation in PRF thermometry in the presence of perfusion decrease and increase can be seen. In the muscle reactive perfusion increases during RF hyperthermia (on the left

side away from the tip). In tumours no or low reactive perfusion is expected, showing very good accuracy ($<1^{\circ}\text{C}$) between fiber optic measurements and PRF thermometry. At the tumor margin perfusion declines (at the tip of the catheter), probably caused by the adjacent hyperperfused muscle (steal effect).

190x357mm (96 x 96 DPI)

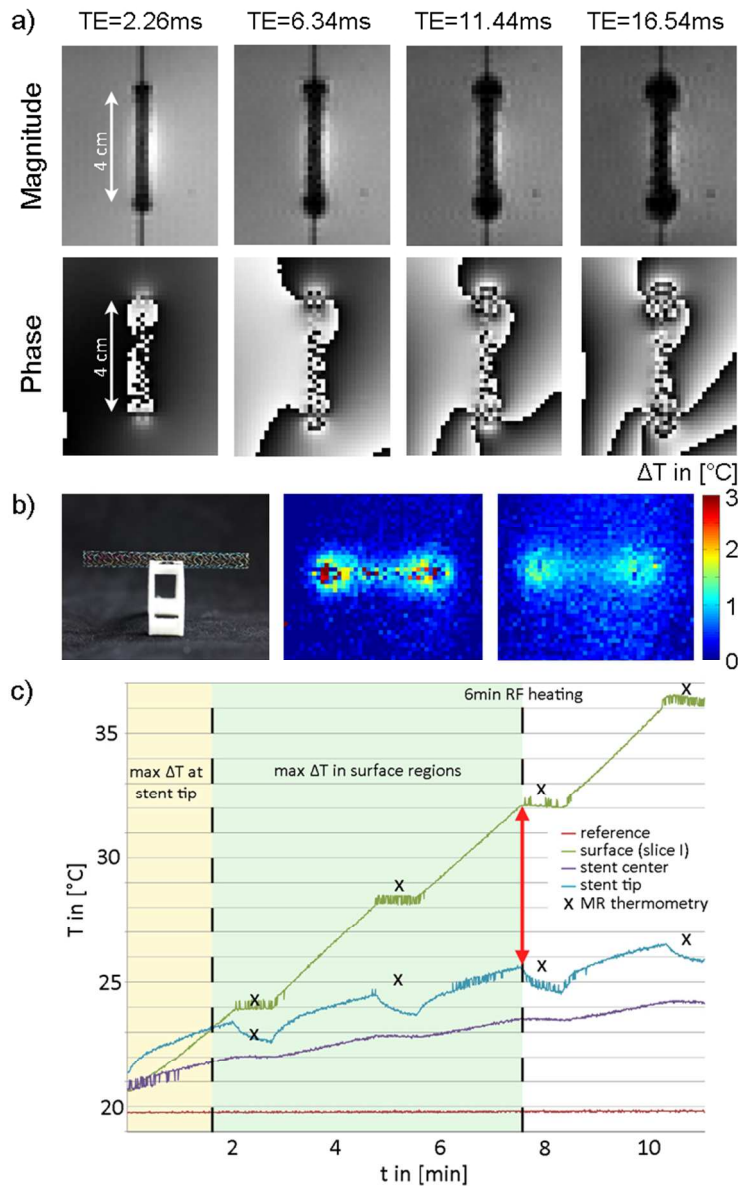


Figure 2: a) Echo time dependent magnitude and phase images at 7.0T of a coronary stent placed in an agar phantom. Please note how signal voids and phase wraps evolve with prolonged echo times. b) MR photograph of a coronary stent (left) used in RF heating experiments. PRF thermometry through the plane of the stent (middle) and in the plane slightly above the stent (right) using a double echo method (TE1 and TE2), where imaging artefacts are reduced. c) Comparison of MR thermometry and fiber optic thermometry in regions of the stent and surface regions of a homogeneous phantom (87).
131x213mm (150 x 150 DPI)

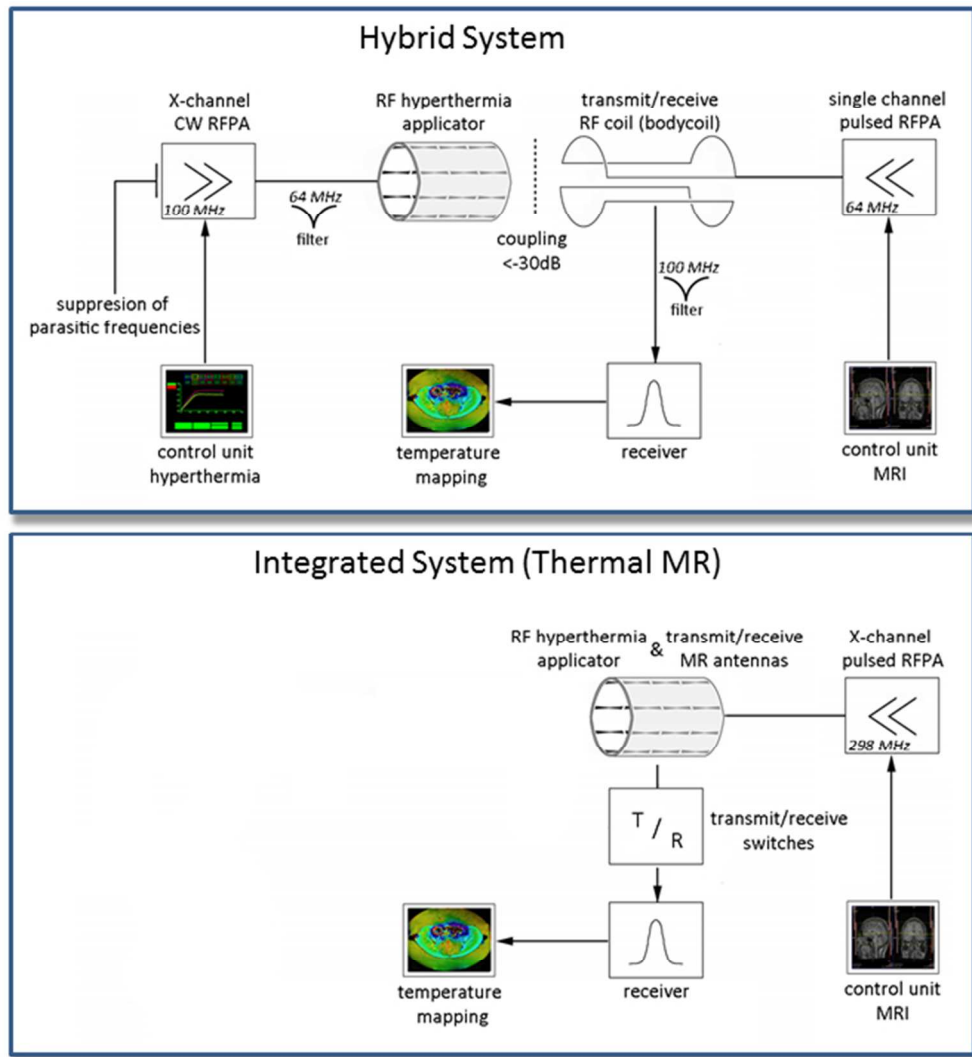


Figure 3: Schematic of a hybrid MR guided RF hyperthermia system (1) and an integrated system presented recently (31). While the hybrid system requires two separate RF amplifiers and control units plus additional hardware filters that need to be incorporated into the standard MR hardware, the integrated system utilizes the proton excitation frequency of the MR system as well as its pulsed power amplifier and control unit to perform RF induced heating. Only transmit receive switches are added to the integrated system, which can be done externally as an integral part of the applicator and does not involve changes in the standard MR architecture itself (31).

178x190mm (96 x 96 DPI)

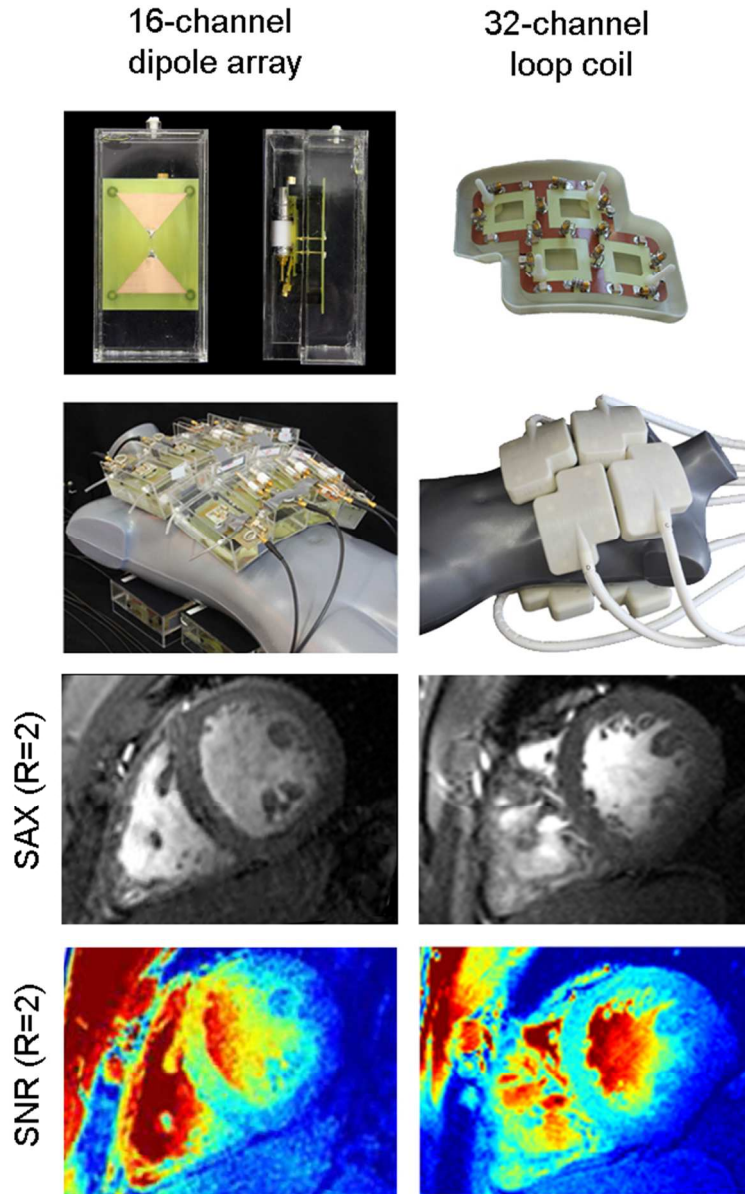


Figure 4: SNR comparison of a 16-channel bow tie dipole array (120) and a 32-channel loop coil array (124) for cardiac imaging at 7.0 T. A 2D CiNE FLASH of a short axis view (SAX) ($1.1 \times 1.1 \times 2.5$ mm²) and its corresponding SNR map (122, 123) is displayed for a GRAPPA reduction factor $R=2$. The 16-channel bow tie dipole array shows higher mean SNR values as compared to the 32-channel loop coil indicating its feasibility for MRI at UHF ($B_0 = 7.0$ T) (120). The excellent image quality obtained from using dipole antennas for MRI demonstrates the rationale of these elements to be used for an integrated system.

111x176mm (150 x 150 DPI)